ACS APPLIED MATERIALS & INTERFACES

Article

Colorimetric Biosensor for Detection of Cancer Biomarker by Au Nanoparticles-Decorated Bi2Se3 Nanosheets

Liangping Xiao, Aimei Zhu, Qingchi Xu, Ying Chen, Jun Xu, and Jian Weng

ACS Appl. Mater. Interfaces, **Just Accepted Manuscript** • DOI: 10.1021/acsami.6b15750 • Publication Date (Web): 06 Feb 2017

Just Accepted

ACS Publications

ACS Applied Materials & Interfaces is published by the American Chemical Society.
1155 Sixteenth Street N.W., Washington, DC 20036

Colorimetric Biosensor for Detection of Cancer Biomarker by Au Nanoparticles-Decorated Bi_2Se_3 Nanosheets

*Liangping Xiao,† Aimei Zhu, *† Qingchi Xu,‡ Ying Chen,⊥ Jun Xu,*‡ and Jian Weng§*

†Department of Chemical & Biochemical Engineering, National Engineering Laboratory for Green Chemical Productions of Alcohols, Ethers and Esters, The College of Chemistry and Chemical Engineering, Xiamen University, Xiamen 361005, China

‡Department of Physics, Research Institute for Biomimetics and Soft Matter, Fujian Provincial Key Laboratory for Soft Functional Materials, Xiamen University, Xiamen, 361005, China

§Department of Biomaterials, Xiamen University, Xiamen, 361005, China

⊥Department of General Surgery, Zhujiang Hospital, Southern Medical University, Guangzhou, 510282, China

Email address: amzhu@xmu.edu.cn; xujun@xmu.edu.cn

ABSTRACT

The colorimetric biosensors have attracted intensive interest, however, their relatively low sensitivity limits their applications in clinic detection. Herein, we develop an effective colorimetric biosensor based on highly catalytic active Au nanoparticle-decorated Bi_2Se_3 (Au/Bi_2Se_3) nanosheets. Au/Bi_2Se_3 nanosheets are facilely synthesized by simply sonicating Au precursor with the as-synthesized Bi_2Se_3 nanosheets in aqueous solution. Owing to the low redox potential and typical topological insulating properties, Bi_2Se_3 nanosheets is capable of providing and accumulating electrons on its surface. Such unique properties of Bi_2Se_3 nanosheets contribute to strong synergistic catalytic effects with Au nanoparticles, particularly when Au/Bi_2Se_3 nanosheets are utilized for catalyzing the reduction of 4-nitrophenol (4-NP) by $NaBH_4$ ($K = 386.67\ s^{-1}g^{-1}$). The excellent catalytic activity of Au/Bi_2Se_3 nanosheets can be "switched off" upon treatment of antibody of cancer biomarker such as anti-carcinoembryonic antibody (anti-CEA). Addition of the corresponding antigen such as cancer biomarker CEA can successively help "switch on" the catalytic activity of Au/Bi_2Se_3 nanosheets, where the resuming degree however depends on the antigen concentration. This cancer biomarker depended catalytic behavior therefore allows Au/Bi_2Se_3 nanosheets to be employed as a colorimetric sensor for detection of a particular cancer biomarker, for the reduction of 4-nitrophenol (4-NP) by $NaBH_4$ itself involves apparent color change. The sensor shows high sensitivity and selectivity for the cancer biomarker, even for a concentration as low as 160 pg/mL for CEA, which fully satisfies

the requirement for real clinical applications. The developed colorimetric sensor shows good generality for detection of different types of cancer biomarkers, such as α-fetoprotein (AFP) and prostate-specific antigen (PSA). Furthermore, real clinic sample analyzing result shows that the prepared biosensor is efficient for detection of CEA, providing an alternative method in cancer diagnosis.

Keywords: Hybrid nanomaterials; catalysis-based colorimetric biosensor; 2D nanomaterials; Cancer diagnosis; Topological insulator

Introduction

With the advances of modern medicine, detection of unusual level of cancer biomarkers, such as carcinoembryonic antigen (CEA), α-fetoprotein (AFP) and prostate-specific antigen (PSA) in clinical samples,[1-6] is usually essential for cancer diagnosis and anti-cancer therapy. So far, most of the reported methods in medical practice for cancer biomarker detection are based on immunoassay techniques, including fluoroimmunoassay,[7] radio immunoassay,[8] enzyme immunoassay[9] and electrochemical immunoassay.[10] Immunoassay is based on the highly specialized recognization activity from a certain pair of antigen and antibody, which provides supreme selectivity over other methods. However, in order to translate the binding information of the antigen-antibody pair into readable signal, most of the developed immunoassay relied on specific labels like fluorescence molecule, radioactive element or enzyme. Technical difficulty of linking such labels to antibody or antigen often makes immunoassay a sophisticated, expensive and time costing process.[11] A facile immunoassay should thus be brought into being to satisfy the expanding demand of cancer biomarker detection.

Among various methods for biomolecule detection,[12-15] colorimetric detection is particularly attractive for its visible radiation, easy operation, and rapid reading.[16,17] The main challenge for development of colorimetric biosensors is to translate invisible signals into color changes. Several strategies have been successfully developed to generate colorimetric signals but challenges still remains. For example, Au nanoparticles (NPs) are widely used as surface

plasmon resonance (SPR)-based colorimetric biosensors due to their outstanding color changing property which however highly determined by the particle size and the particle distance along with the corresponding shift of surface plasmon absorption. Also, electrochemical analysis, another common sensing method, is so sensitive to the experimental environments (such as salt concentration, pH, etc) that false positive signals often occur. Therefore, to overcome the limitations, intense interest has grown in the development of catalysis-based colorimetric biosensors.

Au NPs, owning to their catalytic performances, which can accelerate a certain color-changing reaction to rapidly give visual signals,[18-21] are widely chosen to fabricate colorimeter. However, it still remains challenge to have Au NPs enhance the catalytic performance and resolve the aggregation problem in colloidal system, if bare Au NPs need to be applied on highly sensitive biosensor.[22] A common strategy is to load Au NPs on a proper substrate such as polymer[23,18] metal oxide,[24] or carbon materials.[25] However, most of them merely serve as inert stabilizer to prevent aggregation, while the catalytic property of obtained hybrid nanostructures is not significantly enhanced in comparison to bare Au NPs.[26, 27] More recently, 2D nanomaterials, typically graphene,[28] become popular to support Au NPs to construct catalytic colorimetric biosensor because of their synergistic catalytic effect with Au NPs. Compared with graphene, where electrons fast transfer among the whole 2D nanostructure without direction,[28] topological insulator is supposed to be a better synergist with Au NPs for its interior-insulating

and surface-conducting property, where electrons can only move along the surface.[29-33] Therefore, ultrathin Bi_2Se_3 nanosheet, a typical topological insulator with low redox potential comes into our sight. When hybrid ultrathin Bi_2Se_3 nanosheet with Au NPs, the low redox potential allows the nanosheet to serve as electron donor,[34] and the topological insulating property makes electron transfer efficiently take place only on surface of the nanosheet and the catalyst (Au NPs).[35-37] In consequent, catalytic activity of Au NPs is enhanced to a great extent. Meanwhile, like traditional supporters, ultrathin Bi_2Se_3 nanosheet can also provide abundant surface areas for catalyst (Au NPs) loading without aggregation.[25, 38, 39]

Herein, we develop a facile method for preparation of "naked" Au NPs decorated Bi_2Se_3 nanosheets (Au/Bi_2Se_3). The naked Au NPs realize *in situ* growth on the surface of Bi_2Se_3 nanosheets by simply sonicating Au precursor with the as-synthesized Bi_2Se_3 nanosheets in aqueous solution. As Bi_2Se_3 is capable of providing and accumulating abundant electrons on its surface, the catalytic activity of Au/Bi_2Se_3 hybrid nanostructure is significantly enhanced. The Au/Bi_2Se_3 nanosheets demonstrate pronounced catalytic activity in a model reaction, the reduction of 4-NP (4-nitrophenol) to 4-AP (4-aminophenol) by $NaBH_4$,[18, 40] which offers a colorimetric signal from yellow to colorless. Successive treatment of antigen or antibody shows great potential for antigen/antibody recognition.[41, 42] As shown in scheme 1, for a certain antigen-antibody pair, upon addition of antibody (anti-CEA), Au/Bi_2Se_3 catalysts are "switched off" as adsorption of antibody (anti-CEA) to Au surface inhibited activity of the catalyst. Conversely,

addition of antigen (CEA) will bind with antibody (anti-CEA) located at the surface of Au/Bi_2Se_3. Upon forming anti-CEA/CEA complex, anti-CEA is supposed to undergo conformational change, leading to a weak affinity between the complex and Au/Bi_2Se_3. As a result, anti-CEA/CEA complex will dissociated from surface of Au/Bi_2Se_3 nanosheet, which in turn "switches on" the catalytic reaction. According to color change of the catalytic reaction, determination of CEA concentration realizes. The biosensor shows generality for detection of cancer biomarkers, including AFP and PSA. The detection limit satisfies the real clinic applications. We further demonstrate that the as-synthesized Au/Bi_2Se_3 nanosheet can be used for detection CEA in real clinic samples, showed promising potential for application in clinic cancer diagnosis.

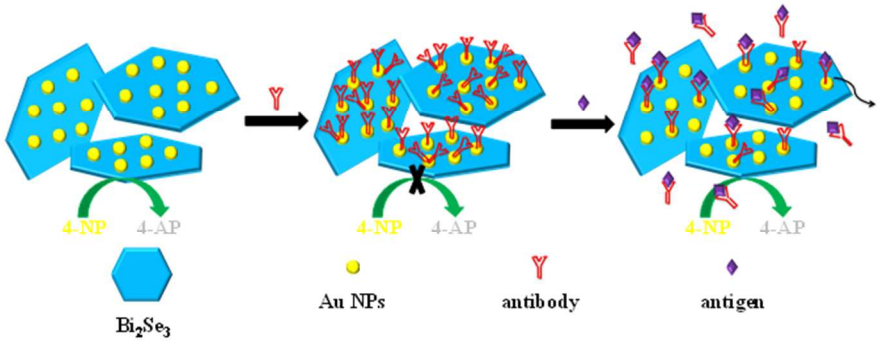

Scheme 1. Schematic illustration of a versatile and colorimetric biosensor based on the tunable smart interface of catalytic Au/Bi_2Se_3 nanosheets.

Results and Discussion

Bi_2Se_3 nanosheets were synthesized according to reported method.[33] The obtained Bi_2Se_3 nanosheets were single or several layers with the uniform size of ~75 nm (Figure 1a). HRTEM image (Figure 1a inserting) reveals the hexagonal lattice fringes with the distance of 0.213 nm, corresponding to (110) plane of the crystal structure of Bi_2Se_3 nanosheets.

Au/Bi_2Se_3 nanosheets were synthesized by sonicating $HAuCl_4$ aqueous solution (20 μL, 4.86 mM) with Bi_2Se_3 nanosheets at room temperature. Figure 1b shows plenty of Au NPs uniformly distributed over the surface of Bi_2Se_3. The lattice fringe of the obtained Au NPs was about 0.238 nm, corresponding to (111) plane of face-centered cubic (*fcc*) Au NPs (Figure 1c). Furthermore, the size of more than 90% of Au NPs was in range of 4~8 nm, and the mean diameter of particle was about 6 nm (Figure S1). The obtained Au/Bi_2Se_3 nanosheets were further characterized by HAADF-STEM element mapping. Figure 1d-g indicate the uniform distribution of Bi (pink) and Se (orange) over whole nanosheets, and decoration of small Au (green) NPs on surface of Bi_2Se_3 nanosheets.

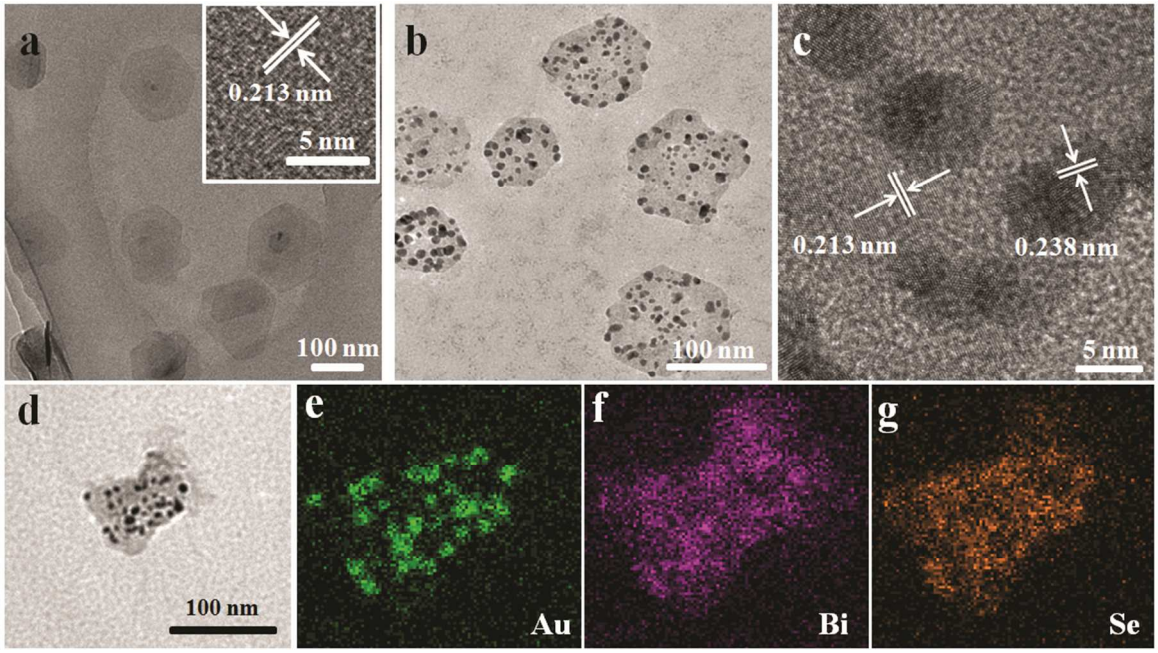

Figure 1. a) TEM image of as-synthesized Bi_2Se_3 nanosheets with inserted HRTEM image of Bi_2Se_3. b) TEM image of Au/Bi_2Se_3 nanosheets. c) HRTEM image of Au/Bi_2Se_3 nanosheets. d-g) HAADF-STEM image and the corresponding elemental mapping of Au/Bi_2Se_3 nanosheets.

XRD characterization of the obtained hybrid nanomaterials also confirms the Au NPs existence. In Figure 2a, XRD pattern of Au/Bi_2Se_3 nanosheets gave a peak at 38.1°, which could be indexed to the (111) crystal faces of *fcc* Au NPs. The peaks at 18.5°, 29.3° and 43.7° corresponded to the (006), (015) and (110) crystal faces of Bi_2Se_3 nanosheets. No diffraction peaks from impurities were detected.

UV-vis absorption spectrum (Figure 2b) of the obtained hybrid nanomaterials displays obvious absorption band at 538 nm, which is attributed to surface plasmon resonance absorption

of Au NPs. Raman spectrum reveals that thickness of the obtained Au/Bi_2Se_3 nanosheets is several nanometers, consisting with the thickness of original Bi_2Se_3 nanosheets (Figure 2c).[31]

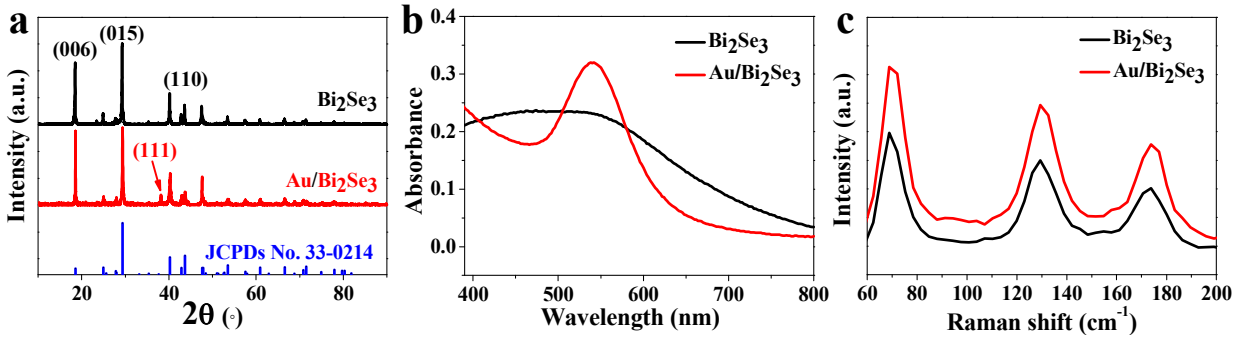

Figure 2. a) XRD patterns of as-synthesized Bi_2Se_3 (black line), Au/Bi_2Se_3 nanosheets (red line) and standard pure Bi_2Se_3 (blue line). b) UV-vis absorption spectra of as-synthesized Bi_2Se_3 nanosheets (black) and Au/Bi_2Se_3 nanosheets (red). c) Raman spectrum of as-synthesized Bi_2Se_3 (black) and Au/Bi_2Se_3 nanosheets (red).

Previous studies have demonstrated that Au NPs could grow on the surface of 2D layered nanomaterials.[43] In most cases, addition of reductants and/or surfactants was necessary, which blockd the catalytic active surface of the obtained hybrid nanostructure.[43,44] However, in our system, without addition of any reductant/surfactant, Au precursor could be reduced into Au NPs on Bi_2Se_3 surface spontaneously.

Initially, we considered that polyvinyl pyrrolidone (PVP) residual on surface of the synthesized Bi_2Se_3 nanosheets involved in Au NPs reduction. However, if PVP stabilized Bi_2Se_3

nanosheets were substituted by exfoliated Bi_2Se_3 nanosheets from bulk Bi_2Se_3 in N-methylpyrrolidone (NMP) without addition of any reagents, Au NPs were observed on the surface of Bi_2Se_3 as well. The uniformly decorated Au NPs on surface of exfoliated Bi_2Se_3 nanosheets (Figure S2) suggested that the residual PVP is not a key factor for Au NPs formation. Therefore, it seems that only Bi_2Se_3 nanosheet is responsible for production of Au NPs.

Although the detailed mechanism is not clarified, the reduction process can be probably attributed to the redox reaction between Bi_2Se_3 and $AuCl_4^-$. Theoretically, the work function of Bi_2Se_3 is 4.2 eV, and the calculated Fermi level of Bi_2Se_3 is higher than the reduction potential of $AuCl^{4-}$ to Au (+1.002 V versus the standard hydrogen electrode). Therefore, it is reasonable to believe that $Bi_2Se_3/AuCl_4^-$ can form a redox pair,[45-47] allowing spontaneous electron transfer from Bi_2Se_3 to $AuCl_4^-$ and consequently result in formation of Au NPs.[48]

X-ray photoelectron spectroscopy (XPS) characterization of the obtained Au/Bi_2Se_3 nanosheets confirms the fact that Bi_2Se_3 induced spontaneous reduction of $AuCl_4^-$. Full-scan XPS spectrum (Figure 3a) suggests that the obtained hybrid nanomaterials are composed of Bi, Se, Au, C, and O, where C and O element, also observed in the original Bi_2Se_3 nanosheets (Figure S3), and could be traced to the ligand on surface of Bi_2Se_3. Figure 3b illustrates valance of Se with a broad peak at 53.9 eV assigning to the 3d level, which, can be further deconvoluted into two peaks: 53.6 eV for $3d_{5/2}$ and 54.2 eV for $3d_{3/2}$ respectively. These signals giving direct evidence of Se^{2-} presence are consistent with the ones in original Bi_2Se_3 nanosheets (Figure S3),

which is also reported in previous studies.[49] A distinctive peak at 58.3 eV in the hybrid nanomaterial corresponded to SeO_x doublets, which is probably ascribed to oxidation of Bi_2Se_3 by $HAuCl_4$ to produce Au NPs.[50, 51] Figure 3c shows Au 4f doublet of the obtained Au/Bi_2Se_3 nanosheets. The Au $4f_{7/2}$ and Au $4f_{5/2}$ were observed at 83.6 eV and 87.4 eV respectively, suggesting Au^0 state existing.[52] Peaks for Bi 4f at 159.2 eV and 164.5 eV remained no change before and after Au NPs growth (Figure 3d and Figure S3), which excluded Bi from Au(III) reduction. Furthermore, a similar spontaneous Au reduction could be carried out when $MoSe_2$ was used instead of Bi_2Se_3, demonstrating that it was Se ions, not Bi ions that dominated the Au(III) reduction (Figure S4).

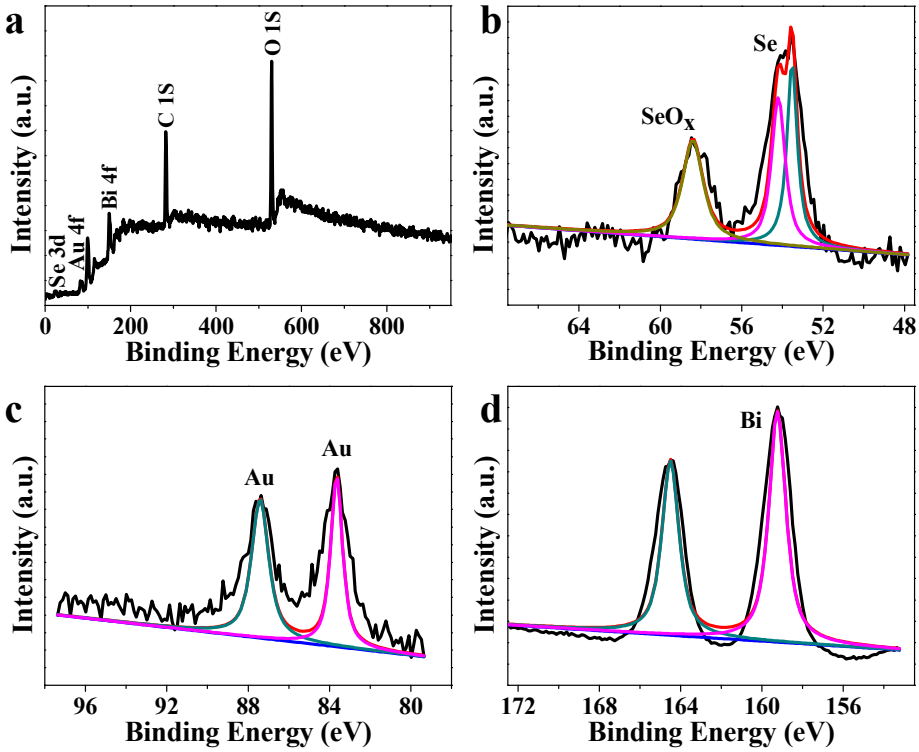

Figure 3. a) Full XPS spectrum of the as-synthesized Au/Bi_2Se_3 nanosheets, and high-resolution XPS spectra of b) Se 3d peaks, c) Au 4f peaks, and d) Bi 4f peaks of Au/Bi_2Se_3 nanosheets.

It is noted that *in situ* growth of Au NPs can severely inhibit homogenous nucleation of Au NPs in solution, and in turn maximize Au NPs density on Bi_2Se_3 nanosheet surface.[53] To confirm this hypothesis, samples with reaction time of 1 min, 10 min and 30 min was characterized by TEM receptively. In the initial stage, it was found that a few small Au NPs (about 4 nm) on surface of Bi_2Se_3 nanosheets and no free Au NPs in solution (Figure S5a), revealing *in situ* nucleation of Au NPs on Bi_2Se_3 surface other than that in solution. As reaction time was prolonged (10 min), size of Au NPs grew and particle density also increased (Figure 1b). Finally, Au NPs with uniform size of about 6 nm (Figure 1b) had a high density on surface of Bi_2Se_3 nanosheet. Further elongation of reaction time did not affect the size or distribution of Au NPs (Figure S5b). The results suggest that Au initially seeded on surface of Bi_2Se_3 and further grow as reaction time increasing until saturated. Control experiment was conducted by introducing a strong reductant such as $NaBH_4$ into the system, which led to homogenous nucleation of Au NPs in solution. As a result, Au NPs were free in solution rather than decorated on Bi_2Se_3 nanosheet (Figure S5c).

To investigate catalytic performance of the obtained Au/Bi_2Se_3 nanosheets, reduction of 4-NP to 4-AP in the presence of excess amount of $NaBH_4$ was chosen as model reaction. The

yellow solution of 4-NP and $NaBH_4$ mixture had a clear UV-vis absorption peak at 400 nm. Absorption signals remained no change if no other actions a taken, indicating no reduction occurring.[54] However, the yellow mixture rapidly faded and ultimately bleached in quick succession once a small amount of Au/Bi_2Se_3 nanosheets (0.018mg) was added (Figure 4a inserting).

The reaction was clearly monitored by time-dependent UV-vis absorption spectra. As shown in Figure 4a, peak at 400 nm disappeared, while a new peak at 300 nm which is a characteristic absorption of reduction product 4-AP appeared gradually, indicating reduction took place under catalysis of Au/Bi_2Se_3 nanosheets. A linear correlation between ln (A) (A is the absorbance intensity at 400 nm) vs. reduction time revealed that the reaction is a pseudo-first-order reaction (Figure 4b). Based on the gradient (Figure 4b), the calculated rate constant (k) was 6.96×10^{-3} s^{-1}. In order to compare the catalytic efficiency with other catalyst, the activity factor **K** is taken into account according to its definition: **K**=k/m, where k stands for rate constant and m refers to total weight of catalyst. The activity factor **K** of Au/Bi_2Se_3 nanosheets is 6.96×10^{-3} s^{-1}/(0.018mg) = 386.67 $s^{-1}g^{-1}$, which is 12 times larger than the previously reported values for Au/graphene hydrogel,[40] and much higher than that of other catalysts (Table 1). Therefore, these results shows that Au/Bi_2Se_3 nanosheet has a high catalytic activity.

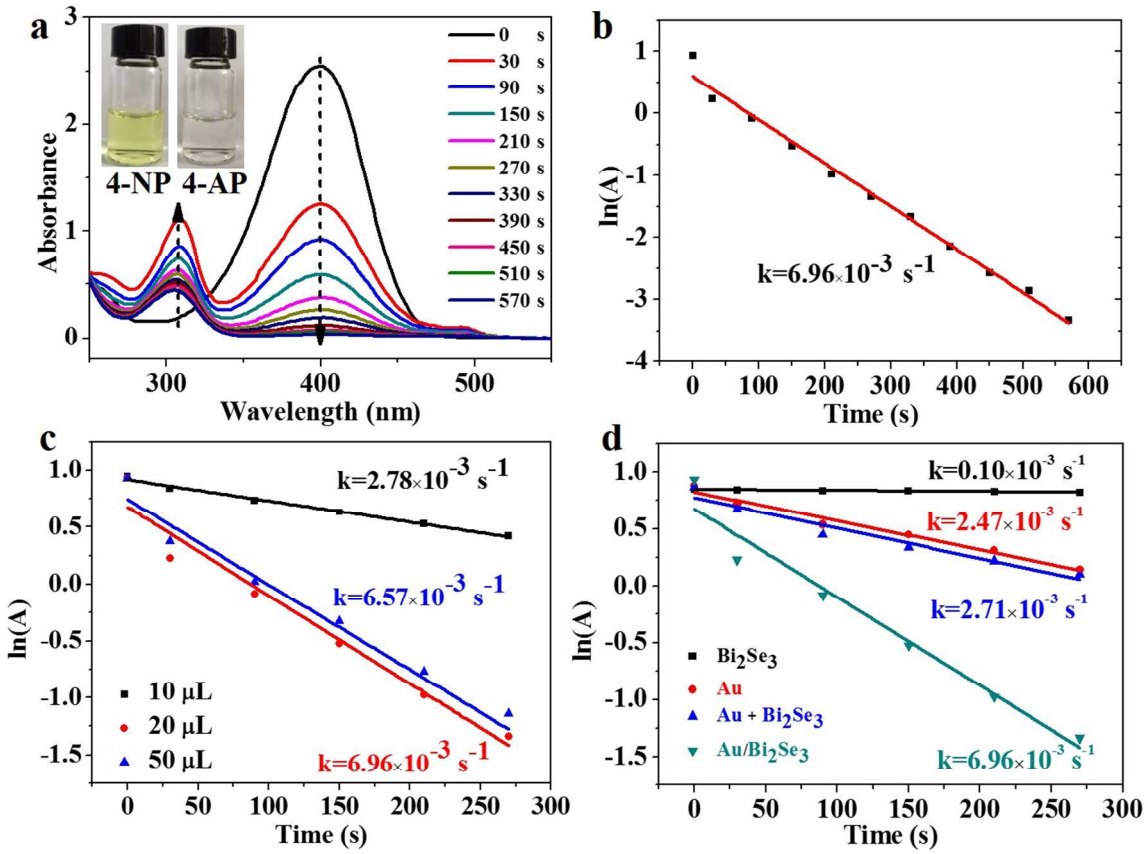

Figure 4. a) UV-vis absorption spectra of the reduction of 4-NP by $NaBH_4$ in the presence of Au/Bi_2Se_3 nanosheets, with inserted photograph showing color change of reduction of 4-NP. b) Plot of ln (A) versus time for the reduction of 4-NP. c) Plot of ln (A) versus time for the reduction of 4-NP in the presence of Au/Bi_2Se_3 nanosheets synthesized with 10 μL (black line), 20 μL (red line) and 50 μL (blue line) of $HAuCl_4$. Refer to Figure S7 for enlarged TEM images. d) Plot of ln (A) versus time for the reduction of 4-NP with Au/Bi_2Se_3 nanosheets (black plots), Bi_2Se_3 (red plots), Au NPs (green plots), and the mixture of Bi_2Se_3 and Au NP solution (blue plots). Reaction conditions: 4-NP = 0.175 mM, $NaBH_4$= 0.42 M.

Table 1. Comparison of the catalytic activity for reduction of 4-NP between Au/Bi_2Se_3 nanosheets and other reported catalysts in the literature.

Catalysts	Catalyst used (mg)	$K(s^{-1}g^{-1})$	Reference
Spongy Au nanoparticles	6	0.35	[55]
Au/PMMA	0.3	2.26	[18]
Au/Au_2S	2	11.9	[56]
Au/graphene hydrogel	0.1	31.7	[40]
Carbon@Au	0.1	238.98	[57]
Au/Bi_2Se_3	0.018	386.67	This work

Au NPs exhibit prominent catalytic ability in various reactions, thus the highly catalytic activity of the obtained hybrid nanosheets was proposed to be owing to the naked gold NPs. To confirm this, thiol ligand (cysteine) with strong coordination affinity to Au NPs was introduced to passivate naked Au NPs. Results showed that k value of the reduction reaction (4-NP to 4-AP) suffered a great decline to 0.11×10^{-3}/s if Au/Bi_2Se_3 nanosheets were pre-treated with thiol ligand (Figure S6a). It should be emphasized that, in this system, suppression of catalytic activity from thiol ligand only worked on Au NPs, and performance of bared Bi_2Se_3 nanosheets were not affected upon same treatment of thiol ligands (Figure S6b). Therefore, naked Au NPs is demonstrated to be the critical factor for catalytic activity of the obtained Au/Bi_2Se_3 nanosheets.

We further studied the effect of Au NP size on catalytic activity, as well as particles density on surface of Bi_2Se_3. During synthesis of Au/Bi_2Se_3 nanosheet, smaller Au NPs (about 4 nm)

with relatively low particle density were generated on surface of Bi_2Se_3 nanosheets (Figure S7) when 10 μL $HAuCl_4$ solution was added. In this case, although smaller NPs had better catalytic activity, the low Au NPs density provided inadequate catalytic site for the reduction reaction. Thus the catalytic activity of Au/Bi_2Se_3 nanosheets synthesized with low concentration of $HAuCl_4$ is poorer than that of optimized Au/Bi_2Se_3 sample (Figure 4c and Figure S7). On the other hand, when 50 μL $HAuCl_4$ solution was introduced, since particle size increased in synchrony with particle density, catalytic activity declined from large particle size dominated active site increment from particle density. Therefore, Au/Bi_2Se_3 nanosheets synthesized with high concentration of $HAuCl_4$ also presented poorer catalytic performance than optimized Au/Bi_2Se_3 nanosheets (Figure 4c and Figure S7). Such results suggests that Au/Bi_2Se_3 nanosheets synthesized with moderated $HAuCl_4$ (20 μL, 4.86 mM) concentration is optimized for performing catalytic reaction.

As shown in Figure 4d, either Bi_2Se_3 nanosheets or free Au NPs alone demonstrated less catalytic activity than the hybrid Au/Bi_2Se_3 nanosheets. Particularly, simple mixing of Bi_2Se_3 nanosheets with Au NPs solution also exhibited poorer catalytic performance than the Au/Bi_2Se_3 nanosheets, which indicated that the interaction between Au NPs and Bi_2Se_3 nanosheets was necessary to synergetic effect on catalytic performance.[58, 59] Figure S8, S9 shows XPS, and zeta potentials of Au/ Bi_2Se_3 before and after reducing 4-NP. XPS data (Table S1) revealed that the Bi_2Se_3 in Au/Bi_2Se_3 was oxidized to SeO_x while zeta potential dropped from −1.28 to −7.56 mV

after the reaction. XPS and zeta potential data strongly suggests that the weak oxidation of Bi_2Se_3 in Au/Bi_2Se_3 during reduction of 4-NP, which gives evidence of electron-donating role Bi_2Se_3 played in the catalytic process. During the catalytic reaction, Au NPs serves as catalyst and electron transporter. Finally, 4-NP accepts electrons, being reduced to 4-AP. Although catalytic activity of Bi_2Se_3 was not as distinct as Au (Figure 4d), it provided strong synergistic effect on catalytic activity in reduction of 4-NP.

Based on the above results, high catalytic activity arising from the Au/Bi_2Se_3 nanosheets was attributed to follow: (1) naked surface of Au NPs significantly avoided passivation of active site; (2) Bi_2Se_3 contributed to strong synergistic effect on the reduction reaction; (3) Bi_2Se_3 nanosheets provided a platform for Au NPs to uniformly distribute on their surface, which greatly prevented aggregation induced inactivation.

Beyond the high catalytic performance, the obtained Au/Bi_2Se_3 nanosheets exhibited unique feature: the surface could be reversibly switched from “active” to “inactive” upon treatment with antibody such as anti-CEA in solution. Catalytic activity of Au/Bi_2Se_3 nanosheets decreased as antibody (anti-CEA) increased (Figure 5a). The catalytic activity of Au/Bi_2Se_3 nanosheets could drop to 13% when antibody (anti-CEA) concentration was increased to 100 μg/mL. The dramatic dropping of catalytic ability arose from non-specific adsorption of antibody (anti-CEA) onto surface of Au/Bi_2Se_3 nanosheets.

To identify the exact position of Au/Bi_2Se_3 nanosheet that anti-CEA adsorbed onto, the following experiments were performed. The same amount of anti-CEA was incubated with as-synthesized Bi_2Se_3 nanosheets and as-synthesized Au/Bi_2Se_3 nanosheets respectively. After incubation, the supernatant of each reaction was separated via centrifugation, and the amount of anti-CEA in supernatant was quantified by protein assay. It was found that the amount of anti-CEA in supernatant has no significant change after incubation with as-synthesized Bi_2Se_3 nanosheets. However, an obvious deduction of anti-CEA amount was detected after incubating with Au/Bi_2Se_3 nanosheets. The results strongly suggests that anti-CEA probably was adsorbed on Au NPs surface, which led to the decrement of anti-CEA in supernatant. To further confirm this hypothesis, thiol ligand blocked Au/Bi_2Se_3 nanosheets, instead of the as-synthesized Au/Bi_2Se_3 nanosheets, were incubated with anti-CEA. The amount of anti-CEA had no change in supernatant before and after incubation. As thiol ligand has strong affinity to Au NPs to block attachment of anti-CEA onto Au, therefore, this result suggested that anti-CEA majorly adsorbed on surface of naked Au NPs rather than Bi_2Se_3 nanosheet. The bound anti-CEA prevented 4-NP from diffusing and binding to active catalytic sites, where catalytic reaction was “switched off”. Especially, color of the system maintained no change regardless of anti-CEA concentration added, which consequently provided an excellent colorimetric sensing system with low background interference.

Furthermore, in order to identify the driving force for the adsorption of anti-CEA on Au/Bi_2Se_3, we studied the zeta potential variation of the Au/Bi_2Se_3 surface during the adsorption process. As shown in Table S2, the detected zeta potential was -27.0 mV for Bi_2Se_3, and -1.28 mV for Au/Bi_2Se_3 respectively. This was not surprised that Au NP decoration reduced the zeta potential of Bi_2Se_3 compared with the bare surface. Zeta potential for net anti-CEA (in PBS) was -16.4 mV. This highly negatively charged anti-CEA was supposed to be able to bind to Au NP surface via electrostatic interaction. Zeta potential of anti-CEA bound Au/Bi_2Se_3 (Au/Bi_2Se_3/anti-CEA) was measured to be about -20.7 mV. Zeta potential shifted from -1.28 mV for Au/Bi_2Se_3 to -20.7 mV for Au/Bi_2Se_3/anti-CEA confirmed the successful attachment of negatively charged anti-CEA to Au/Bi_2Se_3.

The catalytic activity of Au/Bi_2Se_3 nanosheets could resume upon treated with corresponding antigen (CEA), showing potential for detection of a particular antigen. When CEA was added to the mixture of Au/Bi_2Se_3/anti-CEA, 4-NP and $NaBH_4$, the color of solution changed from yellow to colorless rapidly. Such reaction was clearly illustrated by UV-vis spectra (Figure 5b), indicating the reduction of 4-NP to 4-AP. Importantly, the value of reaction rate constant k was indeed dependent on the concentration of antigen (CEA) (Figure 5c), the calibration plots gave a good linear relationship between k and the logarithm values of antigen (CEA) concentrations in range of 1 ng/mL to 10 μg/mL. The results demonstrates great potential for utilizing Au/Bi_2Se_3 as biosensor for detection of cancer marker CEA, and the detection limit is calculated to be 160

pg/mL.[60] Furthermore, this protocol can easily discriminate specific antigen, making it a promising candidate for future specific antigen bioassays.

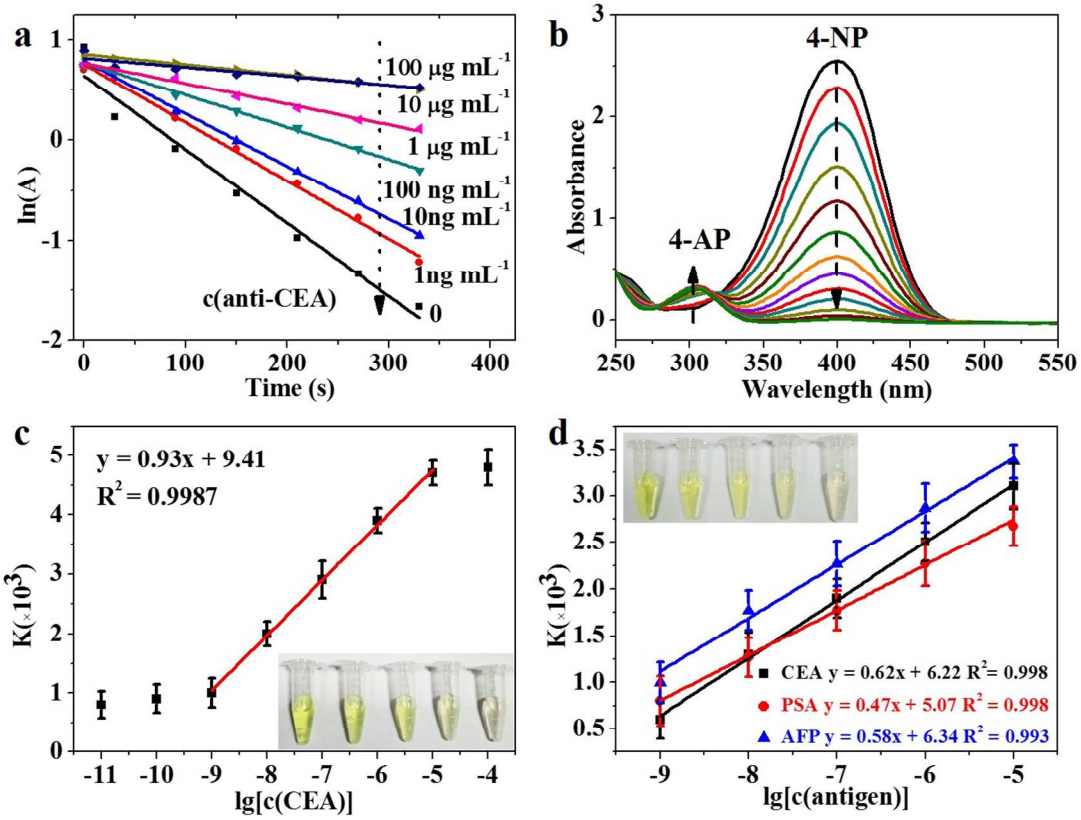

Figure 5. a) Time-dependent absorbance changes at 400 nm of 4-NP reaction solution catalyzed by Au/Bi_2Se_3 nanosheets in the presence of different amounts of anti-CEA. b) UV-vis absorption spectra of the reduction of 4-NP by $NaBH_4$ in the presence of anti-CEA bound Au/Bi_2Se_3 nanosheets and CEA, demonstrating catalytic activity recovery of anti-CEA bound Au/Bi_2Se_3 nanosheets in the presence of CEA. c) The calibration plots showed a good linear relationship between peak currents and the logarithm values of the CEA concentrations. d) The calibration

plots showed a good linear relationship between the reaction constant k and the logarithm values of the CEA concentrations in the media of blood serum. The inset photograph showed color changes of c) PBS solution, and d) normal human serum that containing 4-NP, $NaBH_4$ Au/Bi_2Se_3/anti-CEA upon addition of different concentration of CEA.

We further studied the mechanism of the detection. As the recovery of the catalytic activity must originate from the re-exposure of bare Au active sites, anti-CEA was supposed to be dissociated from surface of Au/Bi_2Se_3. To track anti-CEA, fluorescein isothiocyanate (FITC) conjugated anti-CEA (FITC-anti-CEA) was utilized instead of un-labelled anti-CEA. As shown in Figure S10a, before attachment to Au/Bi_2Se_3, FITC-anti-CEA (green emission) could be detected by confocal laser scanning microscopy (CFLSM) with high intensity (around 60000). Figure S10c, d showed the CFLSM images recorded from the precipitates and supernatant obtained from the mixture of FITC-anti-CEA and Au/Bi_2Se_3 after centrifugation respectively. The decrement in emission intensity of the supernatant (about 12000) in comparison with initial FITC-anti-CEA suggested the successful adsorption of FITC-anti-CEA on surface of Au/Bi_2Se_3. The precipitates, supposed to be composed of Au/Bi_2Se_3/FITC-anti-CEA, did not display sensitive fluorescence due to the quenching effect from Au nanoparticles. The obtained Au/Bi_2Se_3/FITC-anti-CEA was incubated with CEA for 10 min and followed by centrifugation. The supernatant and the precipitates were isolated and characterized by CFLSM respectively.

The supernatant showed intensive green emission with intensity about 18000, while the precipitates did not give significant fluorescence emission. This indicated that green fluorescent component transferred from precipitate to supernatant to form FITC-anti-CEA/CEA complex.

EIS also verified the adsorption of antibody (anti-CEA) on surface of catalyst and the dissociation of antigen-antibody complex. Figure 6a showed the impedance spectra for stepwise modified GCE. Bare GCE gave a straight line, indicating electron-transfer process was not a limiting step of the electrochemical process. Au/Bi_2Se_3 nanosheets modified GCE resulted in a higher electron-transfer resistance (red line in Figure 6a) as Bi_2Se_3 was a typical topological insulator. Adsorption of anti-CEA on Au/Bi_2Se_3 modified GCE created a barrier, which further blocked electron transfer remarkably. Thus, electron-transfer resistance of the anti-CEA/Au/Bi_2Se_3 modified GCE increased significantly (green line in Figure 6a). It was noted that electron-transfer resistance of the anti-CEA modified GCE was not significantly difference from that of bare GCE (orange line in Figure 6a), while electron-transfer resistance of the anti-CEA modified Au/Bi_2Se_3/GCE was increased significantly in comparison with Au/Bi_2Se_3/GCE. Therefore, non-specific adsorption of anti-CEA on GCE was so minor that could be ignored. Immersing anti-CEA/Au/Bi_2Se_3 nanosheets modified electrode in CEA solution resulted in slightly decreasing in the electron-transfer resistance, implying the loss of anti-CEA on surface of Au/Bi_2Se_3 nanosheets (blue line in Figure 6a). The impedance data strongly suggests the

adsorption of anti-CEA on Au/Bi_2Se_3 nanosheets, and desorption of anti-CEA upon treatment with CEA, which is consistence with our proposal.

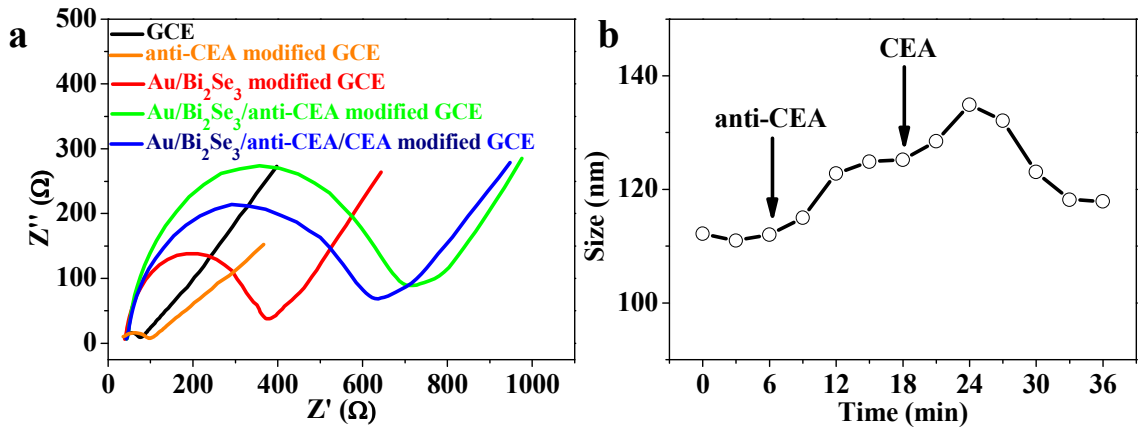

Figure 6. a) Nyquist diagram corresponding to the GCE and the modified GCEs. b) *In situ* DLS measurement of Au/Bi_2Se_3 size evolution in PBS solution with addition of anti-CEA, subsequent purification, and addition of CEA.

To clarify the details of detachment of anti-CEA from the Au/Bi_2Se_3, we monitored the dissociation of anti-CEA by *in situ* Dynamic Light-Scattering (DLS) analysis. As shown in Figure 6b, initial size of Au/Bi_2Se_3 was ~ 112 nm, which increased to 125 nm after incubation with anti-CEA, indicating adsorption of anti-CEA on surface of Au/Bi_2Se_3. The obtained nanohybrids were centrifuged to remove free anti-CEA, and then re-dispersed in PBS for further binding with CEA. After introduction of CEA, size of the nanohybrids was slightly increased to

135 nm, suggesting the successful binding of CEA on surface Au/Bi_2Se_3/anti-CEA via antibody/antigen complex. Size of the nanohybrids then became smaller and finally reached 118 nm, which is slightly larger than the initial Au/Bi_2Se_3 (112 nm as measured). This size decrement can be considered as a strong evidence of dissociation of anti-CEA/CEA complex from surface of Au/Bi_2Se_3.

Actually, there are number of reports proposed significantly conformational changes of antibody (or/and antigen) once antibody/antigen complex formed.[50, 51] Also, conformational changes are known to weaken the affinity between the antibody and the nanoparticles,[61] leading to dissociation of antibody from the nanoparticle. Based on our observation, we proposed the mechanism as following: Initially, CEA bound with anti-CEA on surface of Au/Bi_2Se_3, and tended to form antibody/antigen complex. Upon forming anti-CEA/CEA complex, the induced conformational changes of anti-CEA greatly weakened the affinity between anti-CEA and Au/Bi_2Se_3. Actually, circular dichroism (CD) spectra of Au/Bi_2Se_3/anti-CEA and Au/Bi_2Se_3/anti-CEA/CEA gave significant difference in intensity and shape (Figure S11, and Table S3), indicating conformational changes during anti-CEA/CEA complex formation. As a result, dissociation of anti-CEA/CEA complex from Au/Bi_2Se_3 occurred and active catalytic site exposed.

We further investigated the effects of potentially interfering molecules on the Au/B_2Se_3 nanosheets based colorimetric biosensor. Initially, we found that the recovery of catalytic activity

for Au/Bi_2Se_3/anti-CEA nanosheets was greatly restrained upon treatment with CEA in PBS containing 0.1% albumin (as interfering protein) (Figure S12). This result revealed that the non-specific adsorption of protein on surface of Au/Bi_2Se_3 was a key interference for detection. To avoid this non-specific adsorption from interferent, the detection was performed in diluted system, where the concentration of CEA and the interferent was decreased significantly and interaction between CEA and anti-CEA became dominated. As shown in Figure S12, S13, when target solution was diluted to 1/30 with PBS, a relatively high reaction rate constant k was obtained (82 % of that obtained without interference) and this k had a good linear fit with the logarithm values of antigen (CEA) concentrations. Inadequate dilution gave incomplete inhabitation from interferent, while over dilution on the contrary led to low concentration of CEA. Both effects would significantly influence the detection sensitivity (as shown in Figure S13).

To prove the potential of detection in real clinic samples, we further tried this colorimetric biosensor for CEA detection in real blood serum, which contained a number of biomolecules as interferences. The CEA in desired concentration was added to blood serum. The obtained target blood serum was diluted to 1/30 with PBS, followed by mixing with anti-CEA treated Au/Bi_2Se_3 nanosheets. The calibration plots showed a good linear relationship between the reaction rate constant k and the logarithm values of the CEA concentrations in the range from 1 ng/mL to 10 μg/mL (Figure 5d) with detection limit of 280 pg/mL, and the value of k remained about 65%

(compare to k obtained from detection of pure CEA in aqueous solution). Furthermore, Au/Bi_2Se_3 colorimetric biosensor could be recycled and reutilized for CEA detection even after five times (Figure S14), with a slight decrement in performance quality (judging according to k) after each recycle process arising from anti-CEA and CEA complex adsorption on the surface of Au/Bi_2Se_3.

Although the affinity between anti-CEA and Au/Bi_2Se_3 became weak once anti-CEA/CEA complex formed at surface of Au/Bi_2Se_3, there were still anti-CEA sticking on surface of Au/Bi_2Se_3. This argument could be evidenced by the fact that the recovered catalytic performance of the "re-switched on" system was not so good as the initial Au/Bi_2Se_3 catalyst. After incubation of CEA with Au/Bi_2Se_3/anti-CEA, residue anti-CEA such as non-CEA bound anti-CEA were supposed to leave on surface of Au/Bi_2Se_3, presenting a poorer catalytic performance. The residue anti-CEA on surface of Au/Bi_2Se_3 made Au/Bi_2Se_3 possess high negative charge, where other biomarkers had little affinity to attach on. Therefore, the interfered biomolecules could no longer attach to surface of Au/Bi_2Se_3 even after detachment of anti-CEA/CEA complex.

The generality of Au/Bi_2Se_3 nanosheet based colorimetric biosensor was also investigated. As shown in Figure 5d, Au/Bi_2Se_3 was also applicable to detection of PSA and AFP in blood serum. The calibration plots gave a good linear relationship between k and the logarithm values of PSA concentration or AFP concentration in the range from 1 ng/mL to 10 μg/mL as well. The

detection limit was calculated to be 72 pg/mL for SPA, and 39 pg/mL for AFP respectively. It is interesting that, although blood serum in the clinic sample contained several types of antibody or antigen, which may be also capable of non-specific adsorption onto Au NPs, the corresponding antigen could be identified without significant interference by the established colorimetric biosensor once the selected antibody was pretreated with Au/Bi_2Se_3 nanosheets in the early stage. Therefore, considering the remaining high k value, currently colorimetric assay depicts a promising blueprint for various cancer biomarkers detection in clinic trial.

To prove the biosensor could be applied in clinic diagnosis, three real clinic samples were used to measure CEA concentration, and the results were compared with that obtained from established enzyme-linked immunosorbent assay (ELISA) technique. Each sample was analyzed for three times, and the detailed information was provided in Table 2. Relative errors between the two methods ranged from -4.83% to 1.48%. Thus, it can be considered that no significant difference in the results obtained by the two methods, including positive and negative controls. Furthermore, our method gave a consistent result for CEA concentration in clinic samples, no matter whether standart addition technique was applied or not (Table S4). Results of the detection of real clinic samples strongly illustrate that our biosensor can be applied in the detection of tumor markers and potentially be used for the clinical diagnosis.

Table 2. Results comparison of ELISA and Colorimetric Detection for CEA concentration in real clinic samples.

Serum samples	ELISA (c/ngmL^{-1})	Colorimetric Detection (c/ngmL^{-1})	Relative error (%)
1	2.60	2.63	1.15
2	5.80	5.52	-4.83
3	10.10	10.25	1.48

Conclusions

Au/Bi_2Se_3 hybrid 2D nanosheets were developed by gentle sonication of Au precursor with as-synthesized Bi_2Se_3 nanosheets at room temperature for a few minutes. The obtained hybrids exhibited promising catalytic activity in the reduction of 4-NP by $NaBH_4$. Catalytic activity of the obtained Au/Bi_2Se_3 became "inactive" by treating with antibody, and reversibly turned to "active" upon treatment with corresponding antigen in solution, thus providing a powerful and versatile basis to design a colorimetric biosensor with the Au/Bi_2Se_3 nanosheets. This colorimetric sensor showed great potential in detection of a series of cancer biomarkers, and practical application in detection of clinical sample. Significantly, we envision that the tunable Au/Bi_2Se_3 nanosheets based smart surface could find potential applications in the development of biocatalysis, bioassays, and smart material devices in the future.

Supporting Information

Supporting Information Available: The following files are available free of charge. Materials and methods, Size distribution of Au NPs, XPS spectra of as-synthesized Bi_2Se_3, Characterization of $Au/MoSe_2$ nanosheets, TEM images of as-synthesized Au/Bi_2Se_3 with different reaction parameters, Confocal laser scanning microscopy images of different samples, and zeta potential data, XPS and zeta potential data of Au/Bi_2Se_3 before and after reaction with 4-NP, Circular dichroism spectra of Au/Bi2Se3/anti-CEA and Au/Bi2Se3/anti-CEA/CEA,

Corresponding Author

Email address: amzhu@xmu.edu.cn; xujun@xmu.edu.cn

Author Contributions

The manuscript was written through contributions of all authors. All authors have given approval to the final version of the manuscript.

Acknowledgements

This study is financially supported by National Nature Science Foundation of China (21401153, 31371005), the National Key Scientific Research Projects (2014CB932004), and the Fundamental Research Funds for the Central Universities (20720150016, 20720150017).

.

References

(1) Li, Y. J.; Ma, M. J.; Zhu, J. J., Dual-Signal Amplification Strategy for Ultrasensitive

Photoelectrochemical Immunosensing of Alpha-Fetoprotein. *Anal. Chem.* **2012,** *84*, 10492-10499.

(2) Dai, H.; Yang, C. P.; Tong, Y. J.; Xu, G. F.; Ma, X. L.; Lin, Y. Y.; Chen, G. N., Label-Free Electrochemiluminescent Immunosensor for Alpha-Fetoprotein: Performance of Nafion-Carbon Nanodots Nanocomposite Films as Antibody Carriers. *Chem. Commun.* **2012,** *48*, 3055-3057.

(3) Lilja, H.; Ulmert, D.; Vickers, A. J., Prostate-Specific Antigen and Prostate Cancer: Prediction, Detection and Monitoring. *Nat. Rev. Cancer,* **2008,** *8,*268-278.

(4) Lai, G.; Wu, J.; Ju, H.; Yan, F., Streptavidin-Functionalized Silver-Nanoparticle-Enriched Carbon Nanotube Tag for Ultrasensitive Multiplexed Detection of Tumor Markers. *Adv. Funct. Mater.* **2011,** *21*, 2938-2943.

(5) Perfézou, M.; Turner, A.; Merkoçi, A., Cancer Detection Using Nanoparticle-Based Sensors. *Chem. Soc. Rev.* **2012,** *41*, 2606-2622.

(6) Wu, L.; Qu, X., Cancer Biomarker Detection: Recent Achievements and Challenges. *Chem. Soc. Rev.* **2015,** *44*, 2963-2997.

(7) Yuan, J. L.; Wang, G. L.; Majima, K.; Matsumoto, K., Synthesis of a Terbium Fluorescent Chelate and Its Application to Time-Resolved Fluoroimmunoassay. *Anal. Chem.* **2001,** *73*, 1869-1876.

(8) Sharkey, R. M.; Goldenberg, D. M., Targeted Therapy of Cancer: New Prospects for Antibodies and Immunoconjugates. *Ca-Cancer J. Clin.* **2006,** *56*, 226-243.

(9) Lai, G. S.; Wu, J.; Leng, C.; Ju, H. X.; Yan, F., Disposable Immunosensor Array for Ultrasensitive Detection of Tumor Markers Using Glucose Oxidase-Functionalized Silica Nanosphere Tags. *Biosens. Bioelectron.* **2011,** *26*, 3782-3787.

(10) Kong, F. Y.; Xu, B. Y.; Du, Y.; Xu, J. J.; Chen, H. Y., A Branched Electrode Based Electrochemical Platform: Towards New Label-Free and Reagentless Simultaneous Detection of Two Biomarkers. *Chem. Commun.* **2013,** *49*, 1052-1054.

(11) Volland, H.; Neuburger, L. M.; Schultz, E.; Grassi, J.; Perraut, F.; Creminon, C., Solid-Phase Immobilized Tripod for Fluorescent Renewable Immunoassay. A Concept for Continuous Monitoring of an Immunoassay Including a Regeneration of the Solid Phase. *Anal. Chem.* **2005,** *77*, 1896-1904.

(12) Yola, M. L.; Atar, N., A Novel Voltammetric Sensor Based on Gold Nanoparticles Involved in p-Aminothiophenol Functionalized Multi-Walled Carbon Nanotubes: Application to the Simultaneous Determination of Quercetin and Rutin. *Electrochim. Acta* **2014**, 119, 24-31.

(13) Yola, M. L.; Atar, N.; Eren, T.; Karimi-Maleh, H.; Wang, S., Sensitive and Selective Determination of Aqueous Triclosan Based on Gold Nanoparticles on Polyoxometalate/Reduced Graphene Oxide Nanohybrid. *RSC Adv.* **2015**, 5, 65953-65962.

(14) Yola, M. L.; Eren, T.; Atar, N., A Novel and Sensitive Electrochemical DNA Biosensor Based on Fe@Au Nanoparticles Decorated Graphene Oxide. *Electrochim. Acta* **2014**, 125, 38-47.

(15) Yola, M. L.; Eren, T.; Atar, N.; Saral, H.; Ermiş, İ., Direct-Methanol Fuel Cell Based on Functionalized Graphene Oxide with Mono-Metallic and Bi-Metallic Nanoparticles:

Electrochemical Performances of Nanomaterials for Methanol Oxidation. *Electroanalysis* **2016**, 28, 570-579.
(16) Li, J.; Fu, H. E.; Wu, L. J.; Zheng, A. X.; Chen, G. N.; Yang, H. H., General Colorimetric Detection of Proteins and Small Molecules Based on Cyclic Enzymatic Signal Amplification and Hairpin Aptamer Probe. *Anal. Chem.* **2012,** *84*, 5309-5315.
(17) Song, Y. J.; Qu, K. G.; Zhao, C.; Ren, J. S.; Qu, X. G., Graphene Oxide: Intrinsic Peroxidase Catalytic Activity and Its Application to Glucose Detection. *Adv. Mater.* **2010,** *22*, 2206-2210.
(18) Kuroda, K.; Ishida, T.; Haruta, M., Reduction of 4-Nitrophenol to 4-Aminophenol over Au Nanoparticles Deposited on PMMA. *J. Mol. Catal. A: Chem.* **2009,** *298*, 7-11.
(19) Okumura, M.; Haruta, M., Interplay of Theoretical Calculations and Experiments for a Study of Catalysis by Gold. *Catal. Today* **2016,** *259*, 81-86.
(20) Abad, A.; Concepcion, P.; Corma, A.; Garcia, H., A Collaborative Effect Between Gold and a Support Induces the Selective Oxidation of Alcohols. *Angew. Chem. Int. Edit.* **2005,** *44*, 4066-4069.
(21) Liu, M.; Zhao, H. M.; Chen, S.; Yu, H. T.; Quan, X., Interface Engineering Catalytic Graphene for Smart Colorimetric Biosensing. *ACS Nano* **2012,** *6*, 3142-3151.
(22) Que, X.; Tang, D.; Xia, B.; Lu, M.; Tang, D., Gold Nanocatalyst-Based Immunosensing Strategy Accompanying Catalytic Reduction of 4-Nitrophenol for Sensitive Monitoring of Chloramphenicol Residue. *Anal. Chim. Acta* **2014**, 830, 42-48.
(23) Lee, H. Y.; Shin, S. H. R.; Abezgauz, L. L.; Lewis, S. A.; Chirsan, A. M.; Danino, D. D.; Bishop, K. J. M., Integration of Gold Nanoparticles into Bilayer Structures via Adaptive Surface Chemistry. *J. Am. Chem. Soc.* **2013,** *135*, 5950-5953.
(24) Guan, Y. J.; Hensen, E. J. M., Ethanol Dehydrogenation by Gold Catalysts: The Effect of the Gold Particle Size and the Presence of Oxygen. *Appl. Catal. A* **2009,** *361*, 49-56.
(25) Lv, X.; Weng, J., Ternary Composite of Hemin, Gold Nanoparticles and Graphene for Highly Efficient Decomposition of Hydrogen Peroxide. *Sci. Rep.* **2013,** *3*, 03285.
(26) Sharma, M. K.; Narayanan, J.; Pardasani, D.; Srivastava, D. N.; Upadhyay, S.; Goel, A. K., Ultrasensitive Electrochemical Immunoassay for Surface Array Protein, a Bacillus Anthracis Biomarker Using Au-Pd Nanocrystals Loaded on Boron-Nitride Nanosheets as Catalytic Labels. *Biosens. Bioelectron.* **2016**, 80, 442-449.
(27) Zhao, Y.; Zheng, Y.; Zhao, C.; You, J.; Qu, F., Hollow PDA-Au Nanoparticles-Enabled Signal Amplification for Sensitive Nonenzymatic Colorimetric Immunodetection of Carbohydrate Antigen 125. *Biosens. Bioelectron.* **2015**, 71, 200-206.
(28) Qu, F. L.; Li, T.; Yang, M. H., Colorimetric Platform for Visual Detection of Cancer Biomarker Based on Intrinsic Peroxidase Activity of Graphene Oxide. *Biosens. Bioelectron.* **2011**, 26, 3927-3931.
(29) Peng, J.; Xiong, Y. J.; Lin, Z. Q.; Sun, L. P.; Weng, J., Few-Layer Bismuth Selenides Exfoliated by Hemin Inhibit Amyloid-Beta(1-42) Fibril Formation. *Sci. Rep.* **2015,** *5,* 10171.
(30) Peng, J.; Weng, J., One-Pot Solution-Phase Preparation of a MoS2/Graphene Oxide Hybrid.

Carbon **2015,** *94*, 568-576.
(31) Sun, L.; Lin, Z.; Peng, J.; Weng, J.; Huang, Y.; Luo, Z., Preparation of Few-Layer Bismuth Selenide by Liquid-Phase-Exfoliation and Its Optical Absorption Properties. *Sci. Rep.* **2014,** *4*, 04794.
(32) Waters, J.; Crouch, D.; Raftery, J.; O'Brien, P., Deposition of Bismuth Chalcogenide Thin Films Using Novel Single-Source Precursors by Metal-Organic Chemical Vapor Deposition. *Chem. Mater.* **2004,** *16*, 3289-3298.
(33) Zhang, X.-D.; Chen, J.; Min, Y.; Park, G. B.; Shen, X.; Song, S.-S.; Sun, Y.-M.; Wang, H.; Long, W.; Xie, J.; Gao, K.; Zhang, L.; Fan, S.; Fan, F.; Jeong, U., Metabolizable Bi_2Se_3 Nanoplates: Biodistribution, Toxicity, and Uses for Cancer Radiation Therapy and Imaging. *Adv. Funct. Mater.* **2014,** *24*, 1718-1729.
(34) Cao, W.; Pankratov, V.; Huttula, M.; Shi, X. Y.; Saukko, S.; Huang, Z. J.; Zhang, M., Gold Nanoparticles on MoS2 Layered Crystal Flakes. *Mater. Chem. Phys.* **2015**, 158, 89-95.
(35) Zhang, H.; Liu, C.-X.; Qi, X.-L.; Dai, X.; Fang, Z.; Zhang, S.-C., Topological Insulators in Bi2Se3, Bi2Te3 and Sb2Te3 with a Single Dirac Cone on the Surface. *Nat. Phys.* **2009**, 5, 438-442.
(36) He, K.; Zhang, Y.; He, K.; Chang, C.-Z.; Song, C.-L.; Wang, L.-L.; Chen, X.; Jia, J.-F.; Fang, Z.; Dai, X.; Shan, W.-Y.; Shen, S.-Q.; Niu, Q.; Qi, X.-L.; Zhang, S.-C.; Ma, X.-C.; Xue, Q.-K., Crossover of the Three-Dimensional Topological Insulator Bi2Se3 to the Two-Dimensional Limit. *Nat. Phys.* **2010**, 6, 584-588.
(37) Hong, S. S.; Cha, J. J.; Kong, D.; Cui, Y., Ultra-Low Carrier Concentration and Surface-Dominant Transport in Antimony-Doped Bi2Se3 Topological Insulator Nanoribbons. *Nat. Commun.* **2012**, 3, 757.
(38) Chen, J.; Kuriyama, N.; Yuan, H.; Takeshita, H. T.; Sakai, T., Electrochemical Hydrogen Storage in MoS2 Nanotubes. *J. Am. Chem. Soc.* **2001,** *123*, 11813-11814.
(39) Zhang, B.; Ye, X. C.; Dai, W.; Hou, W. Y.; Xie, Y., Biomolecule-Assisted Synthesis and Electrochemical Hydrogen Storage of Porous Spongelike Ni3S2 Nanostructures Grown Directly on Nickel Foils. *Chem. Eur. J* **2006,** *12*, 2337-2342.
(40) Li, J.; Liu, C.-y.; Liu, Y., Au/Graphene Hydrogel: Synthesis, Characterization and Its Use for Catalytic Reduction of 4-Nitrophenol. *J.Mater. Chem.* **2012,** *22*, 8426-8430.
(41) Liang, L.; Ge, S.; Li, L.; Liu, F.; Yu, J., Microfluidic Paper-Based Multiplex Colorimetric Immunodevice Based on the Catalytic Effect of Pd/Fe(3)O(4)@C Peroxidase Mimetics on Multiple Chromogenic Reactions. *Anal. Chim. Acta* **2015,** *862*, 70-76.
(42) Liu, M.; Jia, C.; Jin, Q.; Lou, X.; Yao, S.; Xiang, J.; Zhao, J., Novel Colorimetric Enzyme Immunoassay for the Detection of Carcinoembryonic Antigen. *Talanta* **2010,** *81*, 1625-1629.
(43) Yin, Z. Y.; Chen, B.; Bosman, M.; Cao, X. H.; Chen, J. Z.; Zheng, B.; Zhang, H., Au Nanoparticle-Modified MoS2 Nanosheet-Based Photoelectrochemical Cells for Water Splitting. *Small* **2014,** *10*, 3537-3543.
(44) Tao, Y.; Ju, E. G.; Ren, J. S.; Qu, X. G., Bifunctionalized Mesoporous Silica-Supported

Gold Nanoparticles: Intrinsic Oxidase and Peroxidase Catalytic Activities for Antibacterial Applications. *Adv. Mater.* **2015,** *27*, 1097-1104.
(45) Choi, H. C.; Shim, M.; Bangsaruntip, S.; Dai, H. J., Spontaneous Reduction of Metal Ions on the Sidewalls of Carbon Nanotubes. *J. Am. Chem. Soc.* **2002,** *124*, 9058-9059.
(46) Kim, J.; Byun, S.; Smith, A. J.; Yu, J.; Huang, J. X., Enhanced Electrocatalytic Properties of Transition-Metal Dichalcogenides Sheets by Spontaneous Gold Nanoparticle Decoration. *J. Phys. Chem. Lett.* **2013,** *4*, 1227-1232.
(47) Kordyuk, A. A.; Kim, T. K.; Zabolotnyy, V. B.; Evtushinsky, D. V.; Bauch, M.; Hess, C.; Buchner, B.; Berger, H.; Borisenko, S. V., Photoemission-Induced Gating of Topological Insulators. *Phys. Rev. B* **2011,** *83*, 081303.
(48) Kiriya, D.; Zhou, Y. Z.; Nelson, C.; Hettick, M.; Madhvapathy, S. R.; Chen, K.; Zhao, P. D.; Tosun, M.; Minor, A. M.; Chrzan, D. C.; Javey, A., Oriented Growth of Gold Nanowires on MoS2. *Adv. Funct. Mater.* **2015,** *25*, 6257-6264.
(49) Das, B.; Sarkar, D.; Maity, S.; Chattopadhyay, K. K., Ag Decorated Topological Surface State Protected Hierarchical Bi_2Se_3 Nanoflakes for Enhanced Field Emission Properties. *J. Mater. Chem. C* **2015,** *3*, 1766-1775.
(50) Kong, D. S.; Cha, J. J.; Lai, K. J.; Peng, H. L.; Analytis, J. G.; Meister, S.; Chen, Y. L.; Zhang, H. J.; Fisher, I. R.; Shen, Z. X.; Cui, Y., Rapid Surface Oxidation as a Source of Surface Degradation Factor for Bi_2Se_3. *ACS Nano* **2011,** *5*, 4698-4703.
(51) Golyashov, V. A.; Kokh, K. A.; Makarenko, S. V.; Romanyuk, K. N.; Prosvirin, I. P.; Kalinkin, A. V.; Tereshchenko, O. E.; Kozhukhov, A. S.; Sheglov, D. V.; Eremeev, S. V.; Borisova, S. D.; Chulkov, E. V., Inertness and Degradation of (0001) Surface of Bi_2Se_3 Topological Insulator. *J. Appl. Phys.* **2012,** *112*, 113702.
(52) Li, F. H.; Yang, H. F.; Shan, C. S.; Zhang, Q. X.; Han, D. X.; Ivaska, A.; Niu, L., The Synthesis of Perylene-Coated Graphene Sheets Decorated with Au Nanoparticles and Its Electrocatalysis Toward Oxygen Reduction. *J. Mater. Chem.* **2009,** *19*, 4022-4025.
(53) Huang, X.; Zeng, Z. Y.; Bao, S. Y.; Wang, M. F.; Qi, X. Y.; Fan, Z. X.; Zhang, H., Solution-Phase Epitaxial Growth of Noble Metal Nanostructures on Dispersible Single-Layer Molybdenum Disulfide Nanosheets. *Nat. Commun.* **2013,** *4*,2472.
(54) Hayakawa, K.; Yoshimura, T.; Esumi, K., Preparation of Gold-Dendrimer Nanocomposites by Laser Irradiation and Their Catalytic Reduction of 4-Nitrophenol. *Langmuir* **2003,** *19*, 5517-5521.
(55) Rashid, M. H.; Bhattacharjee, R. R.; Kotal, A.; Mandal, T. K., Synthesis of Spongy Gold Nanocrystals with Pronounced Catalytic Activities. *Langmuir* **2006,** *22*, 7141-7143.
(56) Gadgil, B.; Damlin, P.; Viinikanoja, A.; Heinonen, M.; Kvarnström, C., One-Pot Synthesis of an Au/Au2S Viologen Hybrid Nanocomposite for Efficient Catalytic Applications. *J. Mater. Chem. A* **2015,** *3*, 9731-9737.
(57) Zhang, P.; Shao, C. L.; Li, X. H.; Zhang, M. Y.; Zhang, X.; Su, C. Y.; Lu, N.; Wang, K. X.; Liu, Y. C., An Electron-Rich Free-Standing Carbon@Au Core-Shell Nanofiber Network as a

Highly Active and Recyclable Catalyst for the Reduction of 4-Nitrophenol. *Phys. Chem. Chem. Phys.* **2013,** *15*, 10453-10458.

(58) Liang, Y. Y.; Li, Y. G.; Wang, H. L.; Zhou, J. G.; Wang, J.; Regier, T.; Dai, H. J., Co3O4 Nanocrystals on Graphene as a Synergistic Catalyst for Oxygen Reduction Reaction. *Nat. Mater.* **2011,** *10*, 780-786.

(59) Guo, Y. J.; Deng, L.; Li, J.; Guo, S. J.; Wang, E. K.; Dong, S. J., Hemin-Graphene Hybrid Nanosheets with Intrinsic Peroxidase-Like Activity for Label-Free Colorimetric Detection of Single-Nucleotide Polymorphism. *ACS Nano* **2011,** *5*, 1282-1290.

(60) Weng, J.; Zhang, Z. W.; Sun, L. P.; Wang, J. A., High Sensitive Detection of Cancer Cell with a Folic Acid-Based Boron-Doped Diamond Electrode Using an AC Impedimetric Approach. *Biosens. Bioelectron.* **2011**, 26, 1847-1852.

(61) Davies, D. R.; Cohen, G. H., Interactions of Protein Antigens with Antibodies. *Proc. Natl. Acad. Sci.* **1996**, 93, 7-12.

(62) Garcia, K. C.; Degano, M.; Pease, L. R.; Huang, M. D.; Peterson, P. A.; Teyton, L.; Wilson, I. A., Structural Basis of Plasticity in T Cell Receptor Recognition of a Self Peptide MHC Antigen. *Science* **1998**, 279, 1166-1172.

(63) Mahmoudi, M.; Lynch, I.; Ejtehadi, M. R.; Monopoli, M. P.; Bombelli, F. B.; Laurent, S., Protein-Nanoparticle Interactions: Opportunities and Challenges. *Chem Rev.* **2011**, 111, 5610-5637.

For TOC only

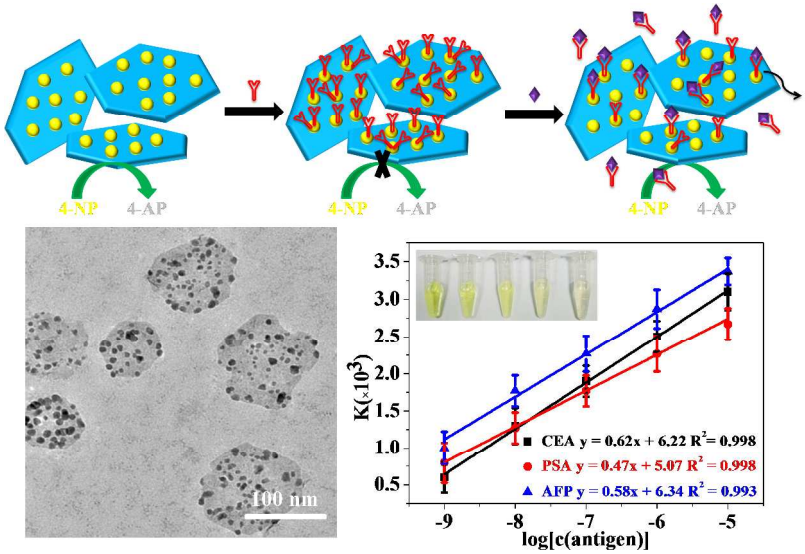
4-NP
4-AP
4-NP
4-AP
4-NP
4-AP
100 nm
K(×10^3)
3.5
3.0
2.5
2.0
1.5
1.0
0.5
-9
-8
-7
-6
-5
log[c(antigen)]
CEA y = 0.62x + 6.22 R² = 0.998
PSA y = 0.47x + 5.07 R² = 0.998
AFP y = 0.58x + 6.34 R² = 0.993